Pandal-Blanco, A.; Pastor Enguídanos, JM.; García Oliver, JM.; Baldwin, E.; Schmidt, D. (2016). A consistent, scalable model for Eulerian spray modeling. International Journal of Multiphase Flow. 83:162-171. doi:10.1016/j.ijmultiphaseflow.2016.04.003.

A Consistent, Scalable Model for Eulerian Spray Modeling

A. Pandal[a,b,*], J.M. Pastor[a], J.M. García-Oliver[a], E. Baldwin[b], D.P. Schmidt[b]

[a] *CMT-Motores Térmicos, Universitat Politècnica de València, Spain*
[b] *Department of Mechanical and Industrial Engineering, University of Massachusetts, Amherst, USA*

Abstract

Despite great practical interest in how sprays emanate from fuel injectors, the near-nozzle region has remained a challenge for spray modelers. Recently, Eulerian models have shown promise in capturing the fast gas-liquid interactions in the near field. However, with the inclusion of compressibility, it can be difficult to maintain consistency between the hydrodynamic and thermodynamic variables. In order to resolve numerical inconsistencies that occur in segregated solutions of Eulerian spray model equations as well as to provide good scalability and stability, a new construction of a Σ-Y model is introduced. This construction is built around an IMEX-RK3 algorithm which offers accuracy and efficiency. The new algorithm is compared to an existing implementation for speed and is validated against experimental measurements of spray evolution in order to test the accuracy. The predictions of the new construction are slightly more accurate and, when tested on 256 processors, 34 times faster.

Keywords: Eulerian, Diesel spray, IMEX-RK3 algorithm, Near-field, CFD, OpenFOAM®

1. Introduction

Fuel injector design is a critical factor in internal combustion engine performance. Unfortunately, the dense spray region just outside of fuel injectors

*Corresponding author
Email address: adpanbla@mot.upv.es (A. Pandal)

remains an enigma. This optically dense space within the first few millimeters of the injector is only penetrable with special diagnostics such as x-ray radiography [21, 22, 39]. This greatly limits the extent to which the flow can be experimentally characterized and leaves scientists with very speculative ideas of how the dense spray region evolves. Furthermore, the computational characterization of this region is challenging due to the complexity of the flow. Here the Reynolds and Weber numbers are very high and the flow typically contains large density ratios, phase change, and often near-supercritical fluids [9]. These factors make the direct numerical simulation of the dense spray region extremely expensive, spurring both industry and academia towards the development of primary atomization models. Although numerous primary atomization models have received wide-spread attention, these models are not necessarily predictive, requiring inputs such as initial drop size and mass and momentum flux.

One common approach to spray modeling treats the liquid phase using a Lagrangian reference frame and the gaseous phase using an Eulerian reference frame. This approach is naturally applied to the relatively independent evolution of isolated droplets in the far-field region. However, problems occur when trying to apply it to the dense spray region. Here the spray spans the whole range of liquid volume fractions, from zero to unity. The Lagrangian particle tracking approach struggles here because nearly all existing drag, collision, breakup, and vaporization models are based on assumptions of near-spherical droplets in a sparse spray, an assumption that simply is not true in the dense spray region.

For the more convoluted evolution of the dense core, a fully Eulerian modeling approach has shown great promise. Not only are numerical challenges with Lagrangian modeling in dense sprays avoided [1], but the physics are also more appropriate. The approaches of Beau, Blokkeel, Demoulin, Lebas, Vallet [3, 5, 10, 11, 26, 51, 52] emphasize the turbulent mixing of the gas and liquid. This is consistent with the observations of Siebers [46, 47, 48], based on numerous experiments, that "the processes of atomization and the ensuing interphase transport of mass and energy at droplet surfaces are not limiting steps with respect to fuel vaporization in DI diesel sprays." So fully Eulerian treatments of the dense spray seem to have both numerical and physical advantages. In addition to this, simulating the liquid phase using an Eulerian reference frame allows for the solution to include both the external spray and the internal nozzle flow, thus capturing the effects of the nozzle geometry and resulting in a more fully predictive model [43, 13, 57].

More recently, work by Oefelein et al. [9, 35, 36] indicates that the in-cylinder conditions for diesel fuel injection are supercritical or near-supercritical. Even if the spray is not quite above the critical point, the elevated temperatures and pressures result in very small surface tension forces and extremely high Weber numbers. Under these conditions, the gas/liquid interface disappears and spray modeling becomes largely an exercise in modeling variable-density turbulent mixing. With the emphasis on turbulent mixing, Eulerian modeling produces good results and is gaining popularity. Recent successful Eulerian treatments include: [3, 4, 5, 10, 11, 12, 14, 19, 25, 26, 32, 34, 38, 43, 50, 54, 56, 57].

These Eulerian models often transition the liquid phase of the spray to the Lagrangian reference frame in the downstream sparse region. These are referred to as ELSA (Eulerian Lagrangian Spray Atomization) models [5, 25]. The focus of the current paper, however, is strictly Eulerian since the Lagrangian phase may not be necessary for high-ambient pressure diesel simulations [12, 19].

Our experience, and that that of others in the field, have revealed some numerical difficulties when the liquid mass transport equation is solved in a compressible context. We have found a tendency of the thermodynamic variables to lose consistency [2, 19], though ad-hoc corrections can minimize the discrepancy.

The root of the problem is that the equations are usually solved in a segregated fashion. For example, conservation of mass is often solved first, due to the presence of density in the other equations. The transport of liquid mass fraction is then likely solved second. However, density and liquid mass fraction are strongly correlated due to the high density ratio between phases. Though the liquid mass fraction largely determines density, the two quantities have been determined through two different equations. Compounding the problems, the later solution of velocity and pressure results in a combination of density, liquid mass fraction, and pressure that are often inconsistent with the equation of state. Other investigators have noted that the order of solving equations impacts the performance of Eulerian multiphase solvers. For example, Payri et al. [38] noted the challenge of calculating fluxes at various points in the time step.

Finally, we wish to move away from the typical elliptic pressure equation that is at the core of many PISO-like algorithms. Large pressure fluctuations occur due to the large density ratio between phases, as will be discussed in the next section. Because of the high velocities prevalent in modern diesel

fuel injection systems, a density-based approach is well-suited to the highly compressible flow that accompanies these sprays.

The specific contribution of this paper will be to propose a new numerical construction, implemented in the OpenFOAM CFD open source c++ library, that resolves past difficulties with maintaining consistency between hydrodynamic and thermodynamic variables in compressible flow. Not only will the new implementation provide some improvements in accuracy, it will also offer benefits in stability and parallel scalability. With the inexorable march towards large, parallel computations, parallel scalability is a key indicator of the future utility of these models.

2. Analysis

The key equation for the transport of liquid fraction is given in Eqn. 1. Here, $\tilde{Y}$, represents the Favre-averaged mass fraction of liquid, convected by the velocity $\vec{U}$ (the tilde representing Favre-averaging is omitted for clarity from vectors). In a finite volume implementation, the fluxes ϕ are the normal component of mass flux at the cell faces. The variable $\bar{\rho}$ is the average density and the right hand side (RHS) of the equation is a consequence of Favre averaging [17, 18].

$$\frac{\partial \bar{\rho}\tilde{Y}}{\partial t} + \vec{\nabla} \cdot \left(\phi \tilde{Y}\right) = -\vec{\nabla} \cdot \bar{\rho}\widetilde{Y'\vec{U}'} \tag{1}$$

The right side of Eqn. 1 is modeled based on several hypotheses [3, 10, 52]. The current work will employ a Boussinesq assumption without loss of generality. Using a standard turbulent diffusion formulation, Eqn. 1 becomes 2.

$$\frac{\partial \bar{\rho}\tilde{Y}}{\partial t} + \vec{\nabla} \cdot \left(\phi \tilde{Y}\right) = \vec{\nabla} \cdot \left(\frac{\mu_t}{Sc_t}\vec{\nabla}\tilde{Y}\right) \tag{2}$$

The key idea is that the mass fraction of liquid evolves according to the model prescribed in this equation. Historically, such models have been applied to turbulent mixing with great success. However, when applied to multiphase mixing, subtle problems appear.

The fundamental reason that problems appear is that the two phases usually have densities that differ by orders of magnitude. Hence, the $\tilde{Y}$ field strongly effects the density field. For immiscible fluids, the two quantities are algebraically related through Eqn. 3.

$$\frac{1}{\bar{\rho}} = \frac{\tilde{Y}}{\rho_l} + \frac{1-\tilde{Y}}{\rho_g} \tag{3}$$

For constant phase densities, ρ_g and ρ_l, this relationship indicates a one-to-one correspondence between density and mass fraction. This correspondence is more complex in compressible formulations where the phase densities are each determined through an equation of state. In either case, the phase densities in addition to Eqns. 2 and 3 completely determine ρ, which is usually calculated from conservation of mass, as in Eqn. 4.

$$\frac{\partial \bar{\rho}}{\partial t} + \vec{\nabla} \cdot (\phi) = 0 \tag{4}$$

Velocity is solved from the momentum equation, shown below in Eqn. 5.

$$\frac{\partial \rho \vec{U}}{\partial t} + \nabla \cdot (\phi \vec{U}) = -\vec{\nabla} p + \vec{\nabla} \cdot \vec{\vec{\tau}} \tag{5}$$

If we consider other variables such as μ_t to be pre-determined, we appear to have a well-posed system. The four unknowns are $\bar{\rho}$, $\tilde{Y}$, $\vec{U}$, and p, and we have four equations. Pressure, the remaining variable, is typically calculated through the projection of velocity into a flux field that satisfies conservation of mass. Thus, inconsistencies in ρ and $\tilde{Y}$ can manifest themselves through large velocity divergence and gradients in pressure.

The exact order in which the equations should be solved is an interesting question that has previously been explored [50, 38]. Eqn. 2 requires density to be known, which would normally be determined through the conservation of mass. However, solving these two equations and ignoring Eqn. 3 can lead to large violations of consistency. Ad-hoc solutions like correcting the value of $\tilde{Y}$ are usually necessary.

Once compressibility is introduced, however, the situation becomes more complicated and potentially less stable. With compressibility, the pure phase densities, ρ_g and ρ_l are now functions of pressure. The equations were solved in the following order in Trask et al. [50]:

1. Conservation of Mass
2. Mass Fraction Evolution
3. Conservation of Momentum
4. Pressure projection
5. Correct Mass Fraction based on Eqn. 3

However, the mass fraction evolution, combined with conservation of mass, determines $\bar{\rho}$ and $\tilde{Y}$, requiring a specific flux field from the pressure projection. When the pressure is calculated to produce this projection, it changes the species densities. Because there is no natural bounding of pressure in a projection method, these changes can be large, requiring internal iteration. Payri et al. [38] observed the requirement of numerous iterations, driving up the expense of their method. Trask's approach [50] can suffer from stability problems and inconsistency of the thermodynamic variables, as was noted by Garcia-Oliver et al. [19].

The difficulty comes from the segregated nature of these pressure-based algorithms. Using a coupled, density-based algorithm would provide a natural means for keeping the fields synchronized. Following a standard Runge-Kutta procedure would offer a formal sequence that determines exactly when fields should be updated that avoids the conundrums that are a consequence of segregated methods. The order of field updates within a substep is immaterial.

An additional benefit of relying on a more explicit formulation, is that parallel scalability should be excellent. The inter-processor communication required for solution of linear systems is greatly reduced. The time step will be smaller with an explicit scheme, but the cost per time step should be greatly reduced. Using a mixture of implicit and explicit (IMEX) methods could potentially offer the best of both approaches. Other advantages are:

1. Convergence issues are avoided by solving pressure explicitly.
2. The temporal order of accuracy can easily be improved over first order.
3. New equations can easily be added to the scheme, cavitation, for example, without substantially disturbing the arrangement of the code.
4. Because only the orthogonal part of fluxes are treated implicitly in OpenFOAM, skewed meshes often create stability problems. The present implementation relies little on implicit fluxing and may offer better tolerance of skewed meshes.

3. Approach

The IMEX-RK3 algorithm is based on the definition of the explicit third order Runge-Kutta (RK3) scheme which is coupled with an implicit second order Crank-Nicolson (CN) scheme for the stiff terms at each Runge-Kutta

substep. The judicious use of implicit treatments avoids the strictest time-step limitations while still maintaining a largely explicit character. This approach is used to solve the following initial-value problem:

$$\frac{\partial y}{\partial t} = f(t, y), \qquad y(t_0) = y_0 \tag{6}$$

There is no unique RK3 scheme. The general representation has the following form:

$$\begin{aligned} y_{n+1} &= y_n + b_1 k_1 + b_2 k_2 + b_3 k_3 \\ k_1 &= h f(t_n, y_n) \\ k_2 &= h f(t_n + c_2 h, y_n + a_{2,1} k_1) \\ k_3 &= h f(t_n + c_3 h, y_n + (a_{3,1} k_1 + a_{3,2} k_2)) \end{aligned} \tag{7}$$

This can be summarized with a *tableau* in the usual Butcher notation [6] as:

c_1	0		
c_2	$a_{2,1}$	0	
c_3	$a_{3,1}$	$a_{3,2}$	0
	b_1	b_2	b_3

To determine the values of each constant, the exact solution of Eqn. 6 is expanded in a Taylor's series and compared with the solution of Eqn. 7 with each k_i term also expanded. After this process, six expressions that a RK3 scheme must satisfy are obtained:

$$\begin{aligned} & b_1 + b_2 + b_3 = 1 \\ & b_2 c_2 + b_3 c_3 = \frac{1}{2} \\ & c_2 = a_{2,1} \\ & c_3 = a_{3,1} + a_{3,2} \\ & b_2 c_2^2 + b_3 c_3^2 = \frac{1}{3} \\ & b_3 c_2 a_{3,2} = \frac{1}{6} \end{aligned} \tag{8}$$

However, with eight unknowns the solution is clearly not unique and two of them must be chosen. The scheme is implemented in the OpenFOAM

CFD open source C++ library [55]. Dividing every time step into three sub-steps using the 'subcycling' utility in OpenFOAM, results in equal sub-step sizes. As a result, the values of the parameters $c_2 = 1/3$ and $c_3 = 2/3$ are fixed. Hence the unknowns take the following values, defining the explicit RK3 scheme which is known as Heun's third order method (RK3-Heun):

$$\begin{array}{c|ccc} 0 & 0 & & \\ 1/3 & 1/3 & 0 & \\ 2/3 & 0 & 2/3 & 0 \\ \hline & 1/4 & 0 & 3/4 \end{array}$$

The implementation of the RK3-Heun method is made in a Predictor-Corrector notation [28] in three steps as follows:

$$\begin{aligned} &1) \quad t_n + c_2 h \\ &\qquad y_{n+c_2} = y_n + a_{2,1} h y'_n \\ &2) \quad t_n + c_3 h \\ &\qquad y_{n+c_3} = y_n + a_{3,1} h y'_n + a_{3,2} h y'_{n+c_2} \\ &3) \quad t_n + h \\ &\qquad y_{n+1} = y_n + b_1 h y'_n + b_2 h y'_{n+c_2} + b_3 h y'_{n+c_3} \end{aligned} \tag{9}$$

In order to construct the IMEX-RK3 scheme Eqn. 6 is first split in the following way:

$$\frac{\partial y}{\partial t} = f(t, y) + g(t, y), \tag{10}$$

where g(t,y) represents the stiff part of the RHS (advanced with the CN scheme) and f(t,y) represents the nonstiff part of the RHS (advanced with the RK3-Heun scheme).

A similar scheme to the classical CN/RK3-Wray [23] is developed using an Explicit Singly Diagonally Implicit (ESDIRK) CN scheme with four stages as in Cavaglieri and Bewly [8]. This means that a first-same-as-last (FSAL) scheme is constructed, where the implicit part of the last stage of one timestep is precisely the implicit part of the first stage of the next timestep. The corresponding Butcher's tableau for this IMEX scheme is written below. Identically as explained in [8], a careful implementation of CN/RK3-Heun IMEX method incorporates only three implicit stages and three explicit stages per timestep, although it was written in four-stage notation.

0	0			
1/3	1/6	1/6		
2/3	1/6	1/3	1/6	
1	1/6	1/3	1/3	1/6
	1/6	1/3	1/3	1/6

0	0			
1/3	1/3	0		
2/3	0	2/3	0	
1	1/4	0	3/4	0
	1/4	0	3/4	0

The numerical solution of the IMEX scheme is updated as follows in every step of the Predictor-Corrector notation:

1. Update the explicit part of the equation (function $f(t, y)$ on Eqn. 10), using the corresponding stage in Eqn. 9.
2. Add the implicit contribution: Solving Eqn. 11 for U^i (example for the velocity field):

$$U^i = U^i_{EX} + \Delta t \sum_{j=1}^{i-1} a^{IM}_{i,j} g(U^j) + \Delta t a^{IM}_{i,i} g(U^i), \text{where i is RK3 stage} \quad (11)$$

Following Vuorinen et al. [53], after every IMEX-RK sub-step the primitive variables such as velocity are updated at the cell centers and boundary conditions are explicitly updated.

Numerical experiments indicated that a classical, fully explicit RK3 scheme was sufficient for most of the transport equations. The IMEX-RK3 scheme is only applied to the liquid mass fraction equation (Eqn. 13 below), solving the turbulent diffusion of mass (second term on the right side of the equation) with the CN implicit scheme while the RK3-Heun explicit scheme is used for solving all the other equations. This mixture of schemes provides minimal use of implicitness while avoiding the strictest stability constraints.

3.1. Model Equations

The model equations for mass conservation, liquid mass fraction transport, momentum, energy (enthalpy) and mean surface interface density (Σ) have to be written in the form of Eqn. 6, as follows:

$$\frac{\partial \bar{\rho}}{\partial t} = -\vec{\nabla} \cdot (\phi) \quad (12)$$

$$\frac{\partial \bar{\rho}\tilde{Y}}{\partial t} = -\vec{\nabla} \cdot \left(\phi \tilde{Y}\right) + \vec{\nabla} \cdot \left(\frac{\mu_t}{Sc_t} \vec{\nabla} \tilde{Y}\right) \quad (13)$$

$$\frac{\partial \rho \vec{U}}{\partial t} = -\nabla \cdot (\phi \vec{U}) - \vec{\nabla} p + \vec{\nabla} \cdot \vec{\vec{\tau}} \tag{14}$$

$$\frac{\partial \bar{\rho} h}{\partial t} = -\vec{\nabla} \cdot (\phi h) + \vec{\nabla} \cdot \left(\alpha_{eff} \vec{\nabla} h \right) + \frac{\partial p}{\partial t} + \vec{U} \cdot \vec{\nabla} p \tag{15}$$

$$\frac{\partial \rho \overline{\Sigma}}{\partial t} = -\vec{\nabla} \cdot \left(\phi \overline{\Sigma} \right) + \vec{\nabla} \cdot \left(D_{\Sigma} \vec{\nabla} \rho \overline{\Sigma} \right) + (A + a) \, \rho \overline{\Sigma} - V_s \rho \overline{\Sigma}^2 \tag{16}$$

where α_{eff} is the effective turbulent thermal diffusivity and D_{Σ} a suitable diffusion coefficient usually taken as the turbulent viscosity over a Schmidt number. A detailed explanation of the different terms in Eq. 16 and an extensive description of the Σ-Y model can be found in [3, 4, 5, 10, 11, 12, 19].

Finally, as explained in Sec. 2, the pressure equation is derived from an equation of state. The gas phase obeys an ideal gas law, while the liquid phase is assumed to have a linear compressibility, denoted by ψ_l

$$\rho_g = \frac{p}{R_g T} = p \psi_g \tag{17}$$

$$\rho_l = \rho_{l,0} + \psi_l (p - p_0) \tag{18}$$

where $\rho_{l,0}$ and p_0 denote reference density and pressures, respectively, about which the equation of state is linearized.

Replacing the above expressions in Eq. 3 and taking into account that the mean liquid volume fraction denoted by $\overline{Y}$ is defined as ($\overline{Y} = \frac{\bar{\rho} \tilde{Y}}{\rho_l}$), the explicit pressure equation is:

$$p = \frac{\bar{\rho} - \overline{Y} (\rho_{l,0} - \psi_l p_0)}{\psi_g (1 - \overline{Y}) + \overline{Y} \psi_l} \tag{19}$$

4. Experimental data

In order to evaluate and validate the new IMEX-RK3 algorithm for spray simulations, the ECN Spray A database [15, 20] has been used. The "Spray A" condition consists of a free diesel spray injected into a quiescent environment, where well-defined boundary conditions and experimental data are available for model validation purposes. The nominal condition for Spray A corresponds to 150 MPa injection pressure, 900 K ambient temperature and a 22.8 kg/m^3 ambient density.

In this case, the Spray A non-evaporating condition is used in order to evaluate the model in terms of the near-field structure (dense region) of diesel sprays, taking advantage of the available x-ray radiography measurements available in the ECN database [21]. This experiment is conducted with the ambient gas at room temperature (303 K) due to the x-ray transparent polymer windows used, which cannot withstand high temperature. Nevertheless, the same ambient density of the nominal evaporating Spray A condition is matched in order to reproduce similar conditions for the spray breakup process, assuming that density is a more critical parameter than pressure for atomization [31]. The main conditions of this experiment are presented in Table 1. Further details about the experimental set-up are provided in [21].

Table 1: Conditions for non-evaporating Spray A experiment

Fuel	n-Dodecane
Ambient composition	100% N2
Injection pressure [MPa]	150
Ambient temperature [K]	303
Ambient density [kg/m^3]	22.8
Fuel injection temperature [K]	343

A detailed internal nozzle geometric characterization has been performed for the injector employed in these experiments, where the main characteristics are presented in Table 2. The nozzle orifice outlet diameter, nozzle orifice inlet diameter, length, and inlet radius are denoted by D_o, D_i, L and r, respectively. The nozzle convergence is described by the k-factor, as defined in [29]. This smooth entrance and strong convergent angle indicate that the nozzle is unlikely to cavitate, providing a simplification of the nozzle/spray connection.

Table 2: Nozzle geometric characteristics for single-hole Spray A ECN injector

Injector Serial#	$D_o[\mu$m]	$D_i[\mu$m]	L/D_o[-]	r/D_o[-]	k-factor
210675	89.4	116	11.5	0.23	2.7

Even though the internal nozzle geometry has some impact on the first millimeters of the spray, in this work only external flow is considered. A basic evaluation case is enough to accomplish the main objective of validating and evaluating the newly implemented solver against the existing one.

5. Results and Discussion

The new construction of the Σ-Y model built around the IMEX-RK3 algorithm is compared for speed and accuracy to an existing implicit implementation [12, 19] based on a PISO algorithm.

5.1. Computational Domain and Model set-up

In order to simulate the single-hole Spray A injector (Serial# 210675) external flow, a fully three-dimensional domain is considered. This computational domain represents a cylindrical spray chamber with 80 mm in length and 50 mm in diameter. The mesh is structured with non-uniform grid resolution, containing regular cells along the nozzle orifice and stretched with an expansion ratio of 1.01 and 1.06 in the axial and radial directions, respectively. This grid consists of around 2.2 million hexahedral cells and it is designed with a similar mesh structure as in [12, 19]. In the present study, in order to accurately reproduce the near nozzle spray structure and especially at close axial positions, i.e. below 1 mm, outlet orifice grid resolution has been increased, after a grid convergence study using 6, 10, 20 and 30 cells along the orifice diameter. Modeling predictions are compared with the x-ray radiography measurements conducted at Argonne National Laboratory. This measurements, conducted in the near nozzle dense region of a diesel spray, provide a variable called the projected mass density of the fuel, which is calculated by a line-of-sight integration along the x-ray beam [21, 39]. A similar procedure is replicated with the simulation data in order to enable fair comparisons against experiments.

In Fig. 1, detailed comparison is made along the transverse direction for the CFD simulations and x-ray radiography data. This comparison is made at 0.1 mm, 2 mm, and 6 mm downstream of the nozzle exit. Note that the experimental profiles have been shifted to be centred at the axis in order to avoid the effect produced by the offset of the orifice outlet with respect to the needle axis present in the single-hole Spray A injector (Serial# 210675). Neglecting these asymmetries present in the nozzle, results depict at 0.1 mm a progressively enhanced performance with mesh refinement and also the achievement of mesh convergence results. Better agreement is also revealed at 2 mm in terms of peak projected density while at 6 mm quite similar predictions are computed by all the grid resolutions. At the sight of the results, clearly the 20 cells orifice diameter resolution mesh is chosen for the following calculations.

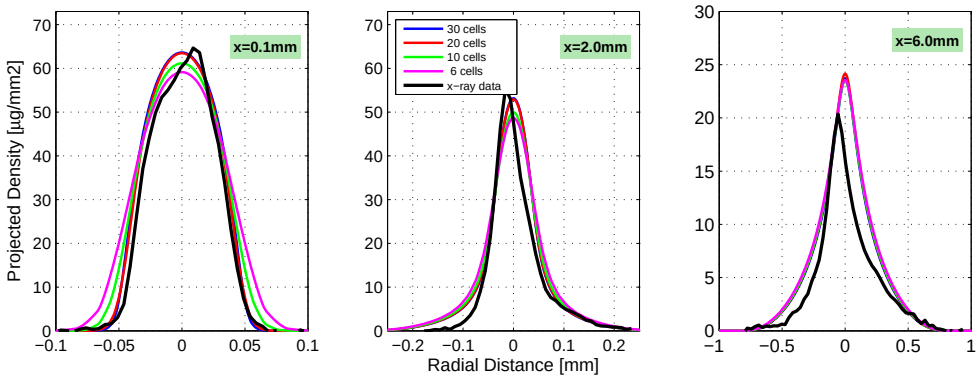

Figure 1: Computed and measured profiles of projected mass density [μg/mm^2] at 500 μs after SOI at axial locations of 0.1 mm, 2 mm, and 6 mm downstream of the nozzle exit. Different orifice mesh resolution

Concerning the boundary conditions, no-slip conditions were selected for all the walls of the domain. A non-reflexive boundary condition is used for the outlet and a time varying velocity condition is used for the inlet. The inlet velocity is obtained from mass flow rate and momentum flux measurements [37], applying a constant radial profile of axial velocity and density at nozzle outlet.

The k-ϵ turbulence model was employed for the simulations. Due to the well known round jet spreading overprediction of k-ϵ type models [40], a corrected value (1.60) for $C_{1\epsilon}$ is used, as indicated in [12, 19]. Pope [40] has previously suggested that the latter value should be used for round jets. The turbulent intensity was set to 5% [12, 19, 24, 30] and the length scale to 10% of the orifice diameter, as suggested in [42] . In any case, the sensitivity to inlet boundary condition turbulence level is studied around these reference values (see Table 3).

Table 3: Turbulence level sensitivity study

Study	Turbulent intensity (It) [%]	Length scale (Lt) [%]
Base	5	10
It2.5	2.5	10
Lt5	5	5

In Fig. 2, projected density profiles are compared again at the three axial locations of 0.1 mm, 2 mm, and 6 mm downstream of the nozzle exit for the

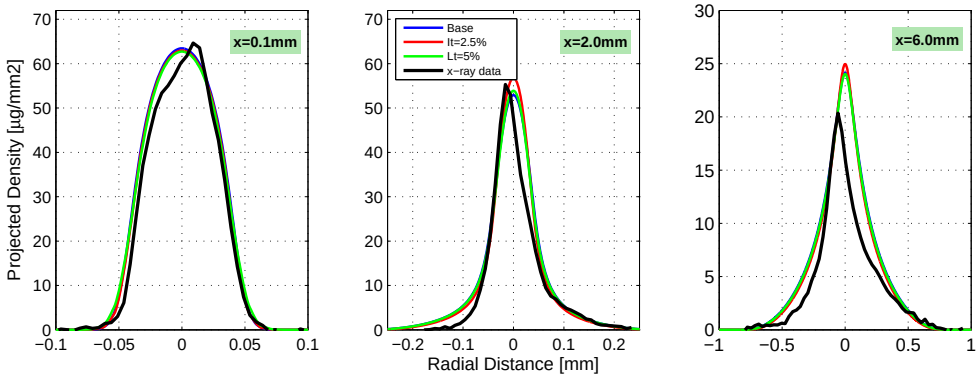

Figure 2: Computed and measured profiles of projected mass density [μg/mm^2] at 500 μs after SOI at axial locations of 0.1 mm, 2 mm, and 6 mm downstream of the nozzle exit. Different turbulence levels

different turbulence levels. Results depict fair agreement with measurements for each of this pair of values investigated, a small impact is notice at 2 mm in terms of peak value but the radial dispersion is equally captured in all simulations and locations. The important outcome of this study is that the conclusions of this work are independent of the turbulence level used as long as suitable values are chosen.

Finally, note that the liquid turbulent flux closure [3] is calculated by means of a gradient closure and the discretization of the divergence terms was solved with a Gamma NVD scheme for both solver approaches. However, a first order Euler scheme is applied for time derivative terms in the case of the existing $\Sigma - Y$ solver [12, 19] while with the IMEX-RK3 algorithm a second order accuracy is achieved.

5.2. Scalability Test

CFD simulations have been conducted making used of the Extreme Science and Engineering Discovery Environment (XSEDE) [49]. Specifically, the computations utilized the TACC Stampede system (at The University of Texas at Austin), which consists of a 10 PFLOPS (PF) Dell Linux Cluster based on 6400+ Dell PowerEdge server nodes, each outfitted with 2 Intel Xeon E5 (Sandy Bridge) processors.

In order to investigate the efficiency of the implementations, several simulations were conducted using different number of processors ($32, 64, 128$ and 256). The parallel speedup comparison is made against the ideal linear scal-

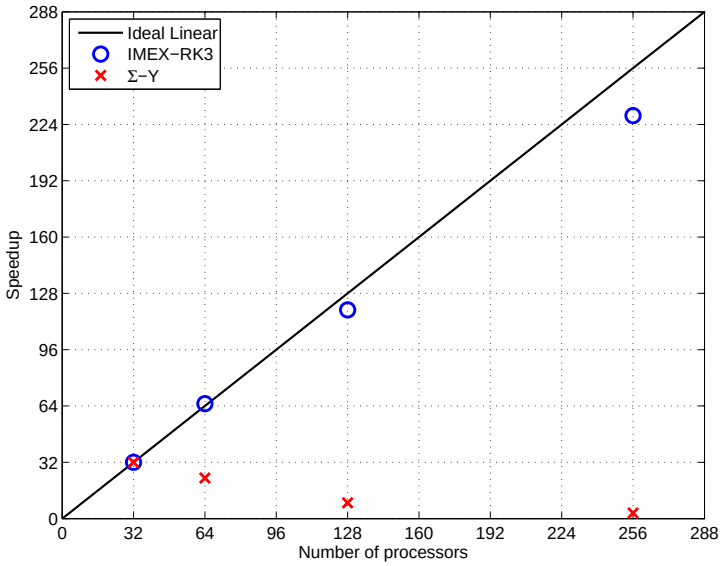

Figure 3: Speedup comparison between both CFD solvers

ability prediction in Fig. 3. The improvement is quite significant; the IMEX-RK3 approach achieves extremely good scalability, scaling linearly down to below 18 thousand cells per core. On the other hand, the previous implicit $\Sigma - Y$ implementation is not able to scale.

OpenFOAM and FOAM-extend employ a no-halo paradigm for parallelization. This paradigm avoids the complexity of maintaining and sharing a set of halo cells that overlap neighboring processor domains, but may require more frequent communication between processors. Some past tests of OpenFOAM scalability have noted poor parallel efficiency [7, 27, 33, 41]. None of these works observed good parallel efficiency beyond 64 processors. Rivera et al. [41] investigated the parallel efficiency in detail, noting that scalability required at least 34,000 cells per processor. They did point out that, with much larger test problems, and with a regular block domain that permits simple decomposition, speedup with up to 1024 processors has been demonstrated in prior work.

In the present work, for situations where the number of cells per processor is very large, the older solver is faster. For example, with only 32 processors, the PISO $\Sigma - Y$ treatment is roughly twice as fast as the new algorithm. However, with 256 processors, the new algorithm is 34 times faster than the PISO algorithm.

5.3. Accuracy Test

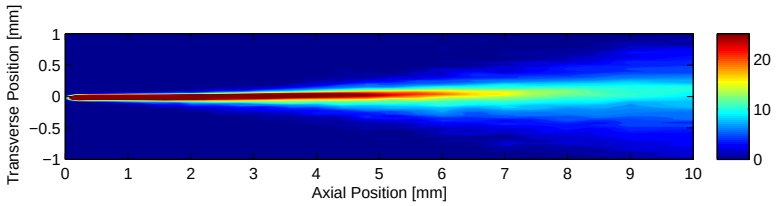

(a) x-ray data

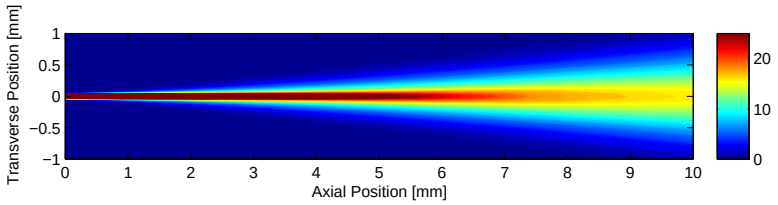

(b) IMEX-RK3 CFD simulation

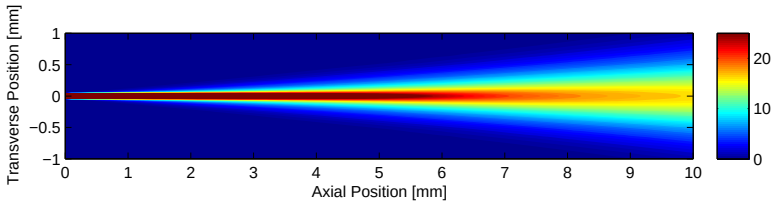

(c) Σ-Y CFD simulation

Figure 4: Projected mass density distributions [μg/mm^2] at 500 μs after SOI from x-ray data and CFD simulations

As previously described, the projected mass density of the fuel from x-ray radiography measurements conducted at Argonne National Laboratory are us is used for comparison. From the projected density contours, Fig. 4, it is seen that both simulations can capture the fuel distribution in the very near nozzle region (i.e., within 6 mm) with both approaches. However, downstream of this axial position, especially further than 8 mm, the IMEX-RK3 solver produces results that are slightly better in terms of peak value, while the radial dispersion of both simulations tend to be over-predicted.

A more detailed comparison is made along the transverse direction comparing the simulations and x-ray radiography data in Fig. 5. The results are not dramatically different and only a slightly lower peak value can be detected in the case of IMEX-RK3 solver predictions in the dense spray re-

gion (0.1 mm, 2 mm). But the differences at 6 mm start to be noticeable, with a peak value prediction by IMEX-RK3 approach almost in the range of experimental data while the base-solver implementation's profile tends to over-predict it. These contrast could be expected due to the results depicted from the projected density contours (Fig. 4). In terms of radial dispersion, results are well matched by both CFD approaches.

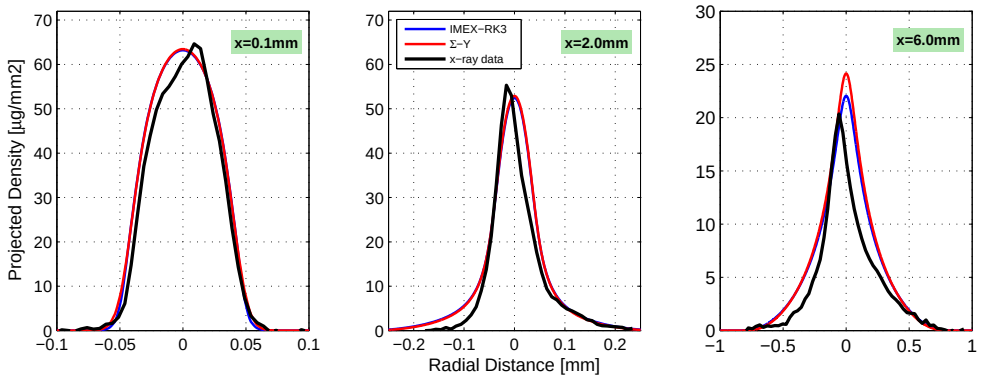

Figure 5: Computed and measured profiles of projected mass density [μg/mm^2] at 500 μs after SOI at axial locations of 0.1 mm, 2 mm, and 6 mm downstream of the nozzle exit

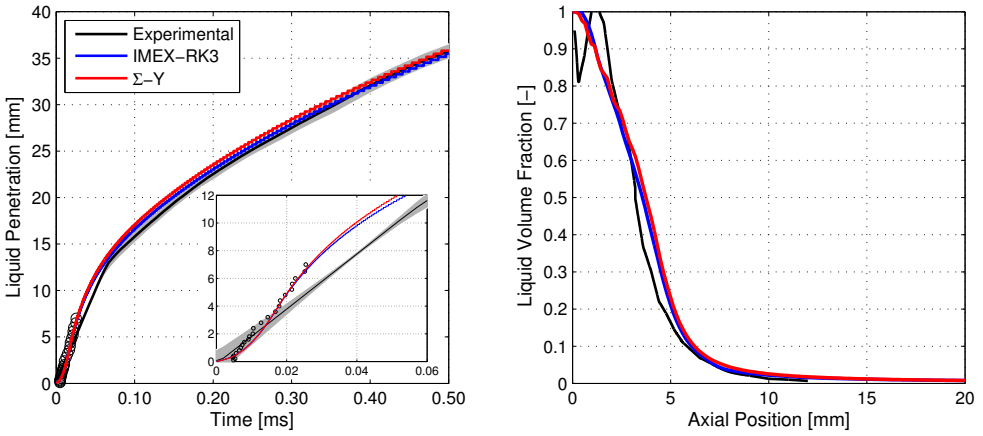

Figure 6: Computed and measured spray penetration [left] and centerline liquid volume fraction at 500 μs after SOI [right]

Apart from the projected mass density variable, a tomographic reconstruction of the radiography data for liquid volume fraction (LVF) was made

by Pickett et al. [39]. These measurements, publicly available at [16], elucidate the effects on the spray dispersion and the intact core length predictions of CFD models. In Fig. 6, the axial profile of the reconstructed liquid volume fraction is compared with CFD computed profiles (right) and a typical characterization spray parameter such as penetration is also evaluated (left). In terms of spray penetration, note in this case that the data are given based on two independent datasets: x-ray radiography from Argonne (black circles) and schlieren imaging from Sandia National Laboratories (black line), showing the limitations of this last technique for capturing the spray within the dense zone near the nozzle exit. In regards to the simulations, both models predict very similar results, although the IMEX-RK3 model is slightly better and seems to fall almost within the experimental uncertainty of measured values. Concerning the LVF axial profiles, the experimental measurements are available only within the first 12 mm. Again the new implementation of the model performs slightly better, predicting a longer intact liquid core ($LVF = 1$), in more agreement with measurements, and a better approximated decay of the liquid volume fraction profile. Discrepancies of the near-nozzle liquid volume profiles with respect to the measurements could be overcome by using a boundary condition from an internal nozzle flow simulation [13]. The effect of using these simulated profiles (not constant at the orifice exit), derived from coupled calculations, prevent the fast mixing process that occurs when using constant inlet profiles, improving the intact core but also with a different decay which match with experimental measurements. Nevertheless, this effects takes place only within 5 mm or 6 mm of the spray and vanishes further downstream, as it has been previously shown in [13].

The tomographic reconstruction is also available for radial profiles at different axial positions, so a more detailed comparison between simulations was made in Fig. 7. Three computed and reconstructed liquid volume fraction radial profiles are compared. The axial locations are the same as in the case of projected mass density analyses ($x = 0.1$ mm, 2 mm and 6 mm downstream of the nozzle exit). It is seen that the radial dispersion at all locations is quite similar for both simulations. However, remarkable differences are depicted in terms of peak value as previously seen in the axial profiles Fig. 6 (right). The most interesting are the greatest differences seen at 6 mm downstream, as shown for the projected mass density in Fig. 5, where the IMEX-RK3 implemented solver clearly outperforms the implicit one. In summary, the IMEX-RK3 solver produces a marginally better simulation due to the density

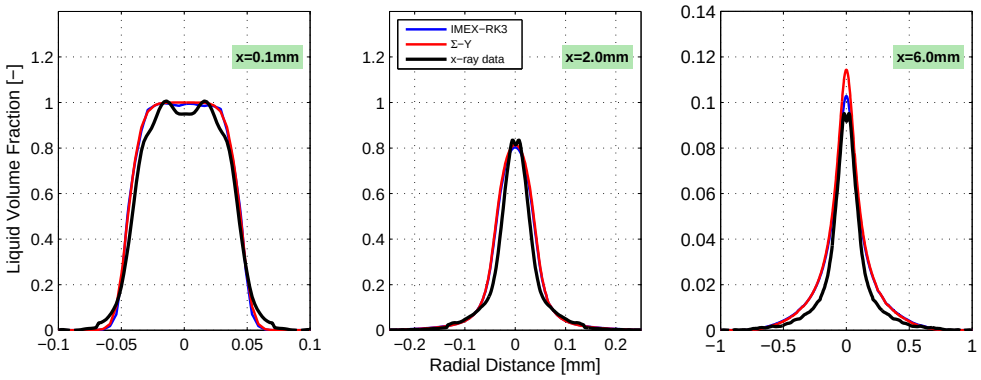

Figure 7: Computed and reconstructed liquid volume fraction radial profiles at 500 μs after SOI at axial locations of 0.1 mm, 2 mm, and 6 mm downstream of the nozzle exit

based solver algorithm keeps the fields better synchronized, which can be seen in the small differences detected in projected density profiles at 6 mm (Fig. 5) and the smoother LVF axial predicted profile (Fig. 6).

Finally, the results were used to check the consistency between variables. This test uses pressure, volume fraction of liquid, and the two pure phase densities to calculate the density. This density represents what would be predicted by the equation of state. However, conservation of mass is used to calculate the actual density in the simulations.

Figure 8 shows the percentage discrepancy between the density of the equation of state and conservation of mass along a transverse section. Three curves are shown, each corresponding to three different numerical methods for simulating compressible Eulerian mixing. The original scheme employed by Trask et al. [50] made no attempt to maintain consistency between these two densities. The second curve represents using an ad-hoc penalty function in the pressure equation. This method, employed by Garcia et al. [19], seems to maintain consistency well. However, the present work maintains even better consistency without any ad-hoc adjustment.

6. Summary and Conclusions

A new solver construction is reported that improves the accuracy, stability, and parallel efficiency of Eulerian spray simulations. This construction is well-suited for large-scale parallel computation of the near-nozzle spray evolution. The wall-clock time for the 256-processor test was about nine

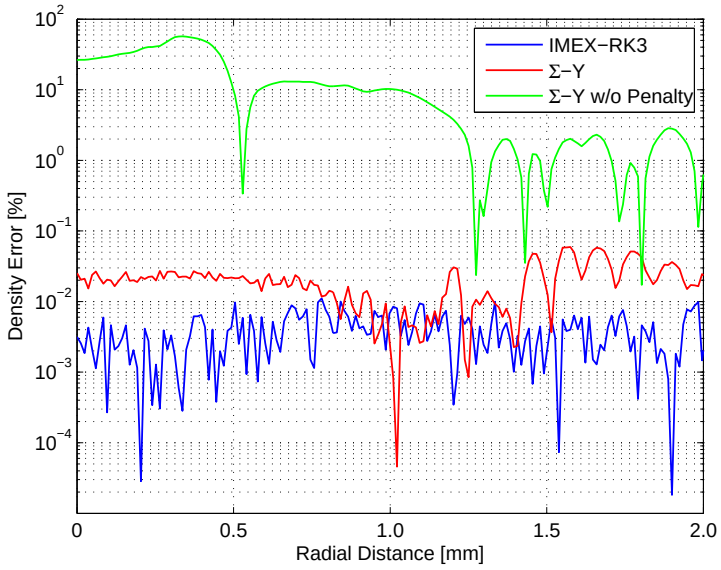

Figure 8: Assessment of consistency between the equation of state and conservation of mass. The three methods correspond to the present work, Garcia-Oliver et al. [19] and Trask et al. [50], respectively

hours, permitting fast enough turn-around for such modeling to be part of a practical injector design cycle. As an additional benefit, validation tests have shown that the predictions are superior to those from a past PISO-based construction.

The use of the Runge-Kutta construction has long-term value, not only for its present performance, but also for its potential. Adding new transport equations, even ones that are tightly coupled to the existing equations, does not require substantial reorganization of the code, because the order in which the equations are solved no longer matters.

Also, the density-based construction is well-suited to handling the high Mach numbers that can occur in bubbly flows, such as cavitation. Hence, this approach shows great potential for inclusion of a cavitation model, which is planned to be included by means of a Homogeneous Relaxation Model (HRM) [44]. For example, Schmidt et al. [45] employed a 3rd order Runge-Kutta construction for simulating cavitation in diesel fuel injector nozzles. Such an extension would be a logical topic for future work. In summary, the new solver shows great promise for future simulations of diesel sprays in the age of peta-scale computing.

Acknowledgement

The authors acknowledge that this work was possible thanks to the Programa de Ayudas de Investigación y Desarrollo (PAID-2013 3198) and Ayudas para Movilidad del Programa para la Formación del Personal Investigador (MovFPI-2014 3931) of the Universitat Politècnica de València.

Also this research used the Extreme Science and Engineering Discovery Environment (XSEDE), which is supported by National Science Foundation grant number ACI-1053575. The authors gratefully acknowledge the computing resources provided on the Texas Advanced Computing Center (TACC) at The University of Texas at Austin that have contributed to the research results reported within this paper. URL: http://www.tacc.utexas.edu

References

[1] Apte, S., Mahesh, K., and Lundgren, T., Accounting for finite-size effects in simulations of disperse particle-laden flows, *International Journal of Multiphase Flow*, vol. **34**, no. 3, pp. 260–271, 2008.

[2] Battistoni, M., Duke, D., Swantek, A., Tilocco, F., Powell, C., and Som, S., Effects of noncondensable gas on cavitating nozzles, *Atomization and Sprays*, vol. **6**, pp. 453–483, 2015.

[3] Beau, P., Funk, M., Lebas, R., and Demoulin, F., Applying quasi-multiphase model to simulate atomization processes in diesel engines: Modeling of the slip velocity, *SAE Technical Paper 2005-01-0220*, 2005.

[4] Beheshti, N., Burluka, A., and Fairweather, M., Assessment of $\Sigma - Y$liq model predictions for air-assisted atomisation, *Theoretical and Computational Fluid Dynamics*, vol. **21**, no. 5, pp. 381–397, 2007.

[5] Blokkeel, G., Barbeau, B., and Borghi, R., A 3D Eulerian model to improve the primary breakup of atomizing jet, *SAE Technical Paper 2003-01-005*, 2003.

[6] Butcher, J. C., Coefficients for the study of Runge-Kutta integration processes, *Journal of the Australian Mathematical Society*, vol. **3**, pp. 185–201, 1963.

[7] Cai, J. and Watanabe, T., Numerical simulation of thermal stratification in cold legs by using openfoam, *Prog Nucl Sci Technol*, vol. **2**, pp. 107–113, 2011.

[8] Cavaglieri, D. and Bewley, T., Low-storage implicit/explicit runge–kutta schemes for the simulation of stiff high-dimensional ODE systems, *Journal of Computational Physics*, vol. **286**, pp. 172 – 193, 2015.

[9] Dahms, R. N., Manin, J., Pickett, L. M., and Oefelein, J. C., Understanding high-pressure gas-liquid interface phenomena in diesel engines, *Proceedings of the Combustion Institute*, vol. **34**, no. 1, pp. 1667 – 1675, 2013.

[10] Demoulin, F., Beau, P., Blokkeel, G., Mura, A., and Borghi, R., A new model for turbulent flows with large density fluctuations: application to liquid atomization, *Atomization and Sprays*, vol. **17**, pp. 315–345, 2007.

[11] Demoulin, F.-X., Reveillon, J., Duret, B., Bouali, Z., Desjonqueres, P., and Menard, T., Toward using direct numerical simulation to improve primary break-up modeling, *Atomization and Sprays*, vol. **23**, no. 11, pp. 957–980, 2013.

[12] Desantes, J., García, J., Pastor, J., and Pandal, A., A comparison of diesel sprays CFD modelling approaches: DDM vs $\Sigma - Y$ eulerian atomization model, *Atomization and Sprays*, vol. **26**, no. 7, pp. 713–737, 2016.

[13] Desantes, J., García, J., Pastor, J., Pandal, A., Baldwin, E., and Schmidt, D., Coupled / decoupled spray simulation comparison of the ECN spray a condition with the $\Sigma - Y$ eulerian atomization model, *International Journal of Multiphase Flow*, vol. **80**, pp. 89 – 99, 2016.

[14] Desportes, A., Zellat, M., Desoutter, G., Liang, Y., and Ravet, F., Application of the Eulerian-Lagrangian spray atomization (ELSA) model for the diesel injection simulation, *THIESEL 2010 Conference on Thermo- and Fluid Dynamic Process in Diesel Engines*, 2010.

[15] ECN, Engine combustion network data archive, 2012.
URL `http://www.sandia.gov/ecn/`

[16] ECN, LVF data archive, 2014.
URL `http://www.sandia.gov/ecn/argonne/assets/datafiles/mixture/rad675.php`

[17] Favre, A. J., Équations des gaz turbulents compressibles, *Journal of Méchanique*, vol. **4**, no. 3, pp. 361–390, 1965.

[18] Favre, A. J., 1969. Statistical equations of turbulent gases. *Problems of Hydrodynamics and Continuum Mechanics*. Soc. for Ind. and Appl. Mathematics, Philadelphia, pp. 231–266.

[19] García-Oliver, J., Pastor, J., Pandal, A., Trask, N., Baldwin, E., and Schmidt, D., Diesel spray CFD simulations based on the $\Sigma - Y$ eulerian atomization model, *Atomization and Sprays*, vol. **23**, pp. 71–95, 2013.

[20] Kastengren, A., Tilocco, F. Z., Powell, C. F., Manin, J., Pickett, L. M., Payri, R., and Bazyn, T., Engine combustion network (ECN):measurements of nozzle geometry and hydraulic behavior, *Atomization and Sprays*, vol. **22**, pp. 1011–1052, 2012.

[21] Kastengren, A. L., , Tilocco, F. Z., Duke, D. J., Powell, C. F., Seoksu, M., and Xusheng, Z., Time-resolved x-ray radiography of diesel injectors from the engine combustion network, *ICLASS Paper*, no. 1369, 2012.

[22] Kastengren, A. L., Powell, C. F., Wang, Y., Im, K.-S., and Wang, J., X-ray radiography measurements of diesel spray structure at engine-like ambient density, *Atomization and Sprays*, vol. **19**, no. 11, pp. 1031–1044, 2009.

[23] Kim, J. and Moin, P., Application of a fractional-step method to incompressible navier-stokes equations, *Journal of Computational Physics*, vol. **59**, no. 2, pp. 308 – 323, 1985.

[24] Lacaze, G., Misdariis, A., Ruiz, A., and Oefelein, J. C., Analysis of high-pressure diesel fuel injection processes using {LES} with real-fluid thermodynamics and transport, *Proceedings of the Combustion Institute*, vol. **35**, no. 2, pp. 1603 – 1611, 2015.
URL `http://www.sciencedirect.com/science/article/pii/S1540748914002302`

[25] Lebas, R., Blokkeel, G., Beau, P., and Demoulin, F., Coupling vaporization model with the Eulerian-Lagrangian spray atomization (ELSA) model in diesel engine conditions, *SAE Technical Paper 2005-01-0213*, 2005.

[26] Lebas, R., Menard, T., Beau, P., Berlemont, A., and Demoulin, F., Numerical simulation of primary break-up and atomization: DNS and modeling study, *International Journal of Multiphase Flow*, vol. **35**, pp. 247–260, 2009.

[27] Liu, X., Parallel modeling of three-dimensional variably saturated ground water flows with unstructured mesh using open source finite volume platform openfoam, *Engineering Applications of Computational Fluid Mechanics*, vol. **7**, no. 2, pp. 223–238, 2013.

[28] Lomax, H., Pulliam, T. H., and Zingg, D. W., *Fundamentals of Computational Fluid Dynamics*, Springer, 2001.

[29] Macián, V., Bermúdez, V., Payri, R., and Gimeno, J., New technique for determination of internal geometry of a diesel nozzles with the use of silicone methodology, *Experimental Techniques*, vol. **37**, pp. 39–43, 2003.

[30] Ménard, T., Tanguy, S., and Berlemont, A., Coupling level set/vof/ghost fluid methods: Validation and application to 3d simulation of the primary break-up of a liquid jet, *International Journal of Multiphase Flow*, vol. **33**, no. 5, pp. 510 – 524, 2007.

[31] Naber, J. and Siebers, D., Effects of gas density and vaporization on penetration and dispersion of diesel sprays, *SAE Technical Paper*, no. 960034, 1996.

[32] Navarro-Martinez, S., Large eddy simulation of spray atomization with a probability density function method, *International Journal of Multiphase Flow*, vol. **63**, pp. 11 – 22, 2014.

[33] Nilsson, H., 2007. Some experiences on the accuracy and parallel performance of openfoam for cfd in water turbines. *Applied Parallel Computing. State of the Art in Scientific Computing*. Springer, pp. 168–176.

[34] Ning, W., Reitz, R., Diwakar, R., and Lippert, A., An eulerian-lagrangian spray and atomization model with improved turbulence modeling, *Atomization and Sprays*, vol. **19**, pp. 727,739, 2009.

[35] Oefelein, J., Dahms, R., and Lacaze, G., Detailed modeling and simulation of high-pressure fuel injection processes in diesel engines, *SAE Int. J. Engines*, vol. **5**, no. 3, p. 10, 2012.

[36] Oefelein, J. C., Dahms, R. N., Lacaze, G., Manin, J. L., and Pickett, L. M., Effects of pressure on the fundamental physics of fuel injection in diesel engines, *ICLASS Paper*, 2012.

[37] Payri, R., García, J., Salvador, F., and Gimeno, J., Using spray momentum flux measurements to understand the influence of diesel nozzle geometry on spray characteristics, *Fuel*, vol. **84**, no. 5, pp. 551 – 561, 2005.

[38] Payri, R., Ruiz, S., Gimeno, J., and Martí-Aldaraví, P., Verification of a new CFD compressible segregated and multi-phase solver with different flux updates-equations sequences, *Applied Mathematical Modelling*, vol. **39**, no. 2, pp. 851 – 861, 2015.

[39] Pickett, L., Manin, J., Kastengren, A., and Powell, C., Comparison of near-field structure and growth of a diesel spray using light-based optical microscopy and x-ray radiography, *SAE Int. J. Engines*, vol. **7**, no. 2, 2014.

[40] Pope, S., An explanation of the turbulent round-jet/plane-jet anomaly, *AIAA*, vol. **16**, pp. 279–281, 1978.

[41] Rivera, O. and Fürlinger, K., Parallel aspects of openfoam with large eddy simulations, *High Performance Computing and Communications (HPCC), 2011 IEEE 13th International Conference on*, IEEE, pp. 389–396, 2011.

[42] Sallam, K. A. and Faeth, G. M., Surface properties during primary breakup of turbulent liquid jets in still air, *AIAA Journal*, vol. **41**, no. 8, pp. 1514–1524, 2003.
URL `http://arc.aiaa.org/doi/abs/10.2514/2.2102`

[43] Salvador, F., Gimeno, J., Pastor, J., and Martí-Aldaraví, P., Effect of turbulence model and inlet boundary condition on the diesel spray behavior simulated by an eulerian spray atomization (ESA) model, *International Journal of Multiphase Flow*, vol. **65**, pp. 108–116, 2014.

[44] Schmidt, D., Gopalakrishnan, S., and Jasak, H., Multi-dimensional simulation of thermal non-equilibrium channel flow, *International Journal of Multiphase Flow*, vol. **36**, no. 4, pp. 284 – 292, 2010.
URL `http://www.sciencedirect.com/science/article/pii/S030193220900192X`

[45] Schmidt, D. P., Rutland, C. J., and Corradini, M. L., A fully compressible, two-dimensional model of small, high-speed, cavitating nozzles, *Atomization and sprays*, vol. **9**, no. 3, 1999.

[46] Siebers, D., Liquid-phase fuel penetration in diesel sprays, *Trans. SAE*, vol. **107**, pp. 1205–1227, 1998.

[47] Siebers, D., Scaling liquid-phase fuel penetration in diesel sprays based on mixing-limited vaporization, *Trans. SAE*, vol. **108**, pp. 703–728, 1999.

[48] Siebers, D. L., 2008. Recent developments on diesel fuel jets under quiescent conditions, *Flow and combustion in reciprocating engines*. Arcoumanis, C. and Kamimoto, T. (Eds.). Springer-Verlag, Berlin, pp. 257–308.

[49] Towns, J., Cockerill, T., Dahan, M., Foster, I., Gaither, K., Grimshaw, A., Hazlewood, V., Lathrop, S., Lifka, D., Peterson, G. D., Roskies, R., Scott, J. R., and Wilkens-Diehr, N., Xsede: Accelerating scientific discovery, *Computing in Science and Engineering*, vol. **16**, no. 5, pp. 62–74, 2014.

[50] Trask, N., Schmidt, D., Lightfoot, M., and Danczyk, S., Compressible modeling of the internal flow in a gas-centered swirl-coaxial fuel injector, *Journal of Propulsion and Power*, vol. **28(4)**, pp. 685–693, 2012.

[51] Vallet, A. and Borghi, R., Modélisation Eulerienne de l'atomisation d'un jet liquide, *C.R. Acad. Sci, Paris*, vol. **327**, pp. 1015–1020, 1999.

[52] Vallet, A., Burluka, A., and Borghi, R., Development of a Eulerian model for the "atomization" of a liquid jet, *Atomization and Sprays*, vol. **11**, pp. 619–642, 2001.

[53] Vuorinen, V., Keskinen, J.-P., Duwig, C., and Boersma, B., On the implementation of low-dissipative runge–kutta projection methods for time dependent flows using openfoam®, *Computers & Fluids*, vol. **93**, pp. 153–163, 2014.

[54] Wang, Y., Lee, W., Reitz, R., and Diwakar, R., Numerical simulation of diesel sprays using an eulerian-lagrangian spray and atomization (ELSA) model coupled with nozzle flow, *SAE Technical Paper 2011-01-0386*, 2011.

[55] Weller, H., Tabor, G., Jasak, H., and Fureby, C., A tensorial approach to computational continuum mechanics using object-oriented techniques, *Computers in Physics*, vol. **12**, pp. 620–631, 1998.

[56] Xue, Q., Battistoni, M., Powell, C., Longman, D., Quan, S., Pomraning, E., Senecal, P., Schmidt, D., and Som, S., An eulerian CFD model and x-ray radiography for coupled nozzle flow and spray in internal combustion engines, *International Journal of Multiphase Flow*, vol. **70**, no. 0, pp. 77 – 88, 2015.

[57] Xue, Q., Battistoni, M., Som, S., Quan, S., Senecal, P. K., Pomraning, E., and Schmidt, D. P., Eulerian cfd modeling of coupled nozzle flow and spray with validation against x-ray radiography data, *SAE Int. J. Engines*, vol. **7(2)**, pp. 1061–1072, 2014.